View metadata, citation and similar papers at core.ac.uk

brought to you by CORE

provided by UNH Scholars' Repository

University of New Hampshire
University of New Hampshire Scholars' Repository

Center for Coastal and Ocean Mapping

Center for Coastal and Ocean Mapping

11-2003

Time dependent seafloor acoustic backscatter (10-100kHz)

Daniel D. Sternlicht
University of California - San Diego

Christian de Moustier
University of California - San Diego

Follow this and additional works at: https://scholars.unh.edu/ccom

Part of the Oceanography and Atmospheric Sciences and Meteorology Commons

Recommended Citation

D. D. Sternlicht and C. P. de Moustier, 'Time-dependent seafloor acoustic backscatter (10–100 kHz)', The Journal of the Acoustical Society of America, vol. 114, no. 5, p. 2709-2725, 2003.

This Journal Article is brought to you for free and open access by the Center for Coastal and Ocean Mapping at University of New Hampshire Scholars' Repository. It has been accepted for inclusion in Center for Coastal and Ocean Mapping by an authorized administrator of University of New Hampshire Scholars' Repository. For more information, please contact nicole.hentz@unh.edu.

Time-dependent seafloor acoustic backscatter (10–100 kHz)[a)]

Daniel D. Sternlicht[b)] and Christian P. de Moustier[c)]
Marine Physical Laboratory, Scripps Institution of Oceanography, University of California at San Diego, La Jolla, California 92093-0205

(Received 1 November 1999; revised 13 June 2003; accepted 26 June 2003)

A time-dependent model of the acoustic intensity backscattered by the seafloor is described and compared with data from a calibrated, vertically oriented, echo-sounder operating at 33 and 93 kHz. The model incorporates the characteristics of the echo-sounder and transmitted pulse, and the water column spreading and absorption losses. Scattering from the water–sediment interface is predicted using Helmholtz–Kirchhoff theory, parametrized by the mean grain size, the coherent reflection coefficient, and the strength and exponent of a power-law roughness spectrum. The composite roughness approach of Jackson *et al.* [J. Acoust. Soc. Am. **79**, 1410–1422 (1986)], modified for the finite duration of the transmitted signal, is used to predict backscatter from subbottom inhomogeneities. It depends on the sediment's volume scattering and attenuation coefficients, as well as the interface characteristics governing sound transmission into the sediment. Estimation of model parameters (mean grain size, roughness spectrum strength and exponent, volume scattering coefficient) reveals ambiguous ranges for the two spectral components. Analyses of model outputs and of physical measurements reported in the literature yield practical constraints on roughness spectrum parameter settings appropriate for echo-envelope-based sediment classification procedures. © *2003 Acoustical Society of America.* [DOI: 10.1121/1.1608018]

PACS numbers: 43.30.Gv, 43.30.Hw, 43.30.Ft, 43.30.Zk [DLB] Pages: 2709–2725

I. INTRODUCTION

In the typical bottom echo-sounding geometry, a sound pulse is transmitted by a sonar system and the time of arrival of the echo provides a measure of the altitude of the sonar above the bottom. However, the shape and duration of the echo are often very different from the original pulse and these distortions contain information about the seafloor acoustic backscattering process as well as the relief and geoacoustic properties of the bottom. By comparing a time-dependent physical model of the acoustic intensity backscattered by the bottom with data from a calibrated echo-sounder operating at 33 and 93 kHz, we intend to infer physical characteristics of the bottom such as the roughness of the water–sediment interface and the mean grain size of the sediment, and geoacoustic properties such as the sediment's volume scattering coefficient and its acoustic impedance.

The bottom echo intensity envelope model described in this paper is a temporal implementation of the SONAR equation,[1,2] based on acoustic backscatter models described in Jackson *et al.*,[3] and analytical tools developed by de Moustier and Alexandrou[4] for modeling seafloor echoes measured with multibeam seafloor mapping sonars. No new theories are presented; rather, a specific combination of physical acoustic backscatter models, geoacoustic parameters, and echo processing techniques is used to estimate the shape and intensity of the average bottom echo envelope measured with simple calibrated echo-sounders. Similar temporal models described by others include: (a) time-dependent representations of surface and volume scattering originally formulated in ''Physics of Sound in the Sea;''[1] (b) temporal seafloor scattering models for swath-mapping sonars developed in Morgera,[5] Morgera and Sankar,[6] and de Moustier and Alexandrou;[4] (c) comprehensive treatment of the time dependence of signals scattered by rough surfaces given by Berry,[7,8] Berry and Blackwell,[9] and Haines and Langston;[10] (d) and, most specifically, average echo envelope models by Nesbitt,[11] Jackson and Nesbitt,[12] de Moustier and Alexandrou,[4] and Pouliquen and Lurton,[13,14] based on combining energy backscattered from the sediment surface and subbottom. Our approach differs from those presented in Refs. 4, 11–14 in its attempt to model and match absolute sound-pressure echo levels measured with a fully calibrated sonar system. Most of the model parameters used are common to Refs. 1–14, with some variations due to choice of physical scattering models detailed herein; however, we propose a specific combination of these parameters in a numerical implementation that incorporates the digitized transmitted waveform, and formulations for reducing the number of geometric dimensions during synthesis of the average backscatter echo envelope. The attempt to obtain absolute backscatter levels related to measurable geoacoustic parameters sets this work apart from mostly phenomenological sediment characterization approaches used in commercial systems,[15,16] which rely on nonparametric classifiers to separate the various substrates, and require independent identification of the substrate by video or core sampling.

At the acoustic wavelengths of interest here (respectively, 4.5 and 1.6 cm at 33 and 93 kHz) the generalized Rayleigh criterion for diffuse scattering of a monochromatic

[a)]Parts of this manuscript were presented at the 137th meeting of the ASA [de Moustier and Sternlicht, J. Acoust. Soc. Am. **105**, 1080 (1999)].

[b)]Current address: Dynamics Technology Inc., 21311 Hawthorne Blvd., Suite 300, Torrance, CA 90503. Electronic mail: dsternlicht@dynatec.com
[c)]Current address: Center for Coastal and Ocean Mapping, University of New Hampshire, 24 Colovos Road, Durham, NH 03824. Electronic mail: cpm@ccom.unh.edu

Redistribution subject to ASA license or copyright; see http://acousticalsociety.org/content/terms. Download to IP: 132.177.229.80 On: Mon, 23 Nov 2015 20:45:01

sound wave, with wavelength λ_a and wave number $k_a = 2\pi/\lambda_a$, on a surface with rms height deviation σ about a mean plane

$$2k_a\sigma \gg 1, \tag{1}$$

implies that the rms height deviations σ must exceed 1 cm. This is satisfied in the data presented here for sandy and silty substrates in San Diego Bay, and we can use a modeling approach based entirely on incoherent scattering. Also, at these frequencies, penetration of the bottom is limited to the first few meters; therefore, assumptions of bottom homogeneity are more likely to be valid. Based on the assumptions that interface scattering dominates the return at normal incidence and volume scattering dominates at oblique incidence, temporal separation of these components is achieved by informed selection of transducer beamwidth and orientation.

The model incorporates the characteristics and geometry of the echo-sounder: the transducer's beam pattern, its altitude, its tilt with respect to vertical, the characteristics of the transmitted sound pulse, and the roll and pitch angles of the platform to which the transducer is mounted; and environmental factors: spherical spreading and absorption losses as the signal propagates through the water column, backscattering of the signal at the water–sediment interface, and by inhomogeneities in the sediment volume.

The mean grain size, defined as ($M_\phi = -\log_2 D_g$) where D_g represents the mean particle diameter in millimeters, is an important component of the sediment's compressional sound speed, saturated bulk density, and attenuation constant, and is of particular interest as it roughly correlates to these parameters through a set of experimentally derived linear regression equations developed by Hamilton[17] and refined by others.[18,19]

Following Jackson *et al.*,[3] Nesbitt,[11] Nesbitt and Jackson,[12] de Moustier and Alexandrou,[4] and Pouliquen and Lurton,[13] the acoustic backscattering at the water–sediment interface and in the sediment volume are modeled and computed independently, then summed to estimate the overall echo intensity measured by the echo-sounder (Fig. 1). Formally, the time-dependent intensity of the bottom backscattered acoustic signal $I(t)$ measured at the transducer's face equals the sum of the intensity $I_i(t)$ backscattered at the water–sediment interface and the intensity $I_v(t)$ backscattered from the sediment volume

$$I(t) = I_i(t) + I_v(t). \tag{2}$$

This paper provides a detailed description of the model and of its sensitivity to changes in its parameters. Data examples are presented with the echo alignment and ensemble averaging processes required to compare measured and modeled echo envelopes. Then, a metric is developed to quantify the closest fit between model and data from which seafloor geoacoustic parameters can be inferred, and the potential for ambiguous results is discussed. The implementation of this model for automatic geoacoustic parameter estimation is the subject of another paper by the authors.[20]

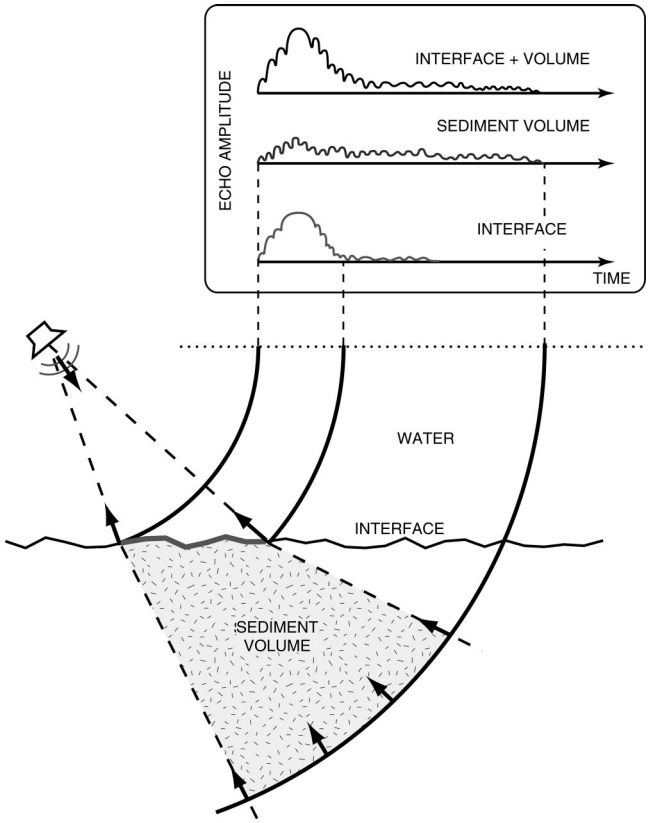

FIG. 1. Separation of acoustic backscatter contributions due to interface roughness and subbottom volume inhomogeneities.

II. MODEL

This section describes the components of Eq. (2), which define the temporal model of high-frequency acoustic seafloor backscatter.

A. Sediment interface characteristics

The analytical form of the signal component backscattered by the water–sediment interface is based on a solution of the Helmholtz diffraction integral for monochromatic sound waves. It uses the Kirchhoff approximation to express the pressure field at planes that are locally tangent to the interface, and the reflection coefficient, $\mathcal{R}(\theta_i)$ at angle of incidence θ_i, is assumed constant at each point on the interface and equal to the normal incidence reflection coefficient $\mathcal{R}_\perp = \mathcal{R}(0)$. The reflection coefficient is a function of the ratios of sediment saturated bulk density over water mass density (ρ) and sediment sound speed over water sound speed (ν)

$$\mathcal{R}(\theta_i) = \frac{\rho\nu\cos(\theta_i) - [1 - (\nu\sin(\theta_i))^2]^{1/2}}{\rho\nu\cos(\theta_i) + [1 - (\nu\sin(\theta_i))^2]^{1/2}}. \tag{3}$$

Given that we are concerned with acoustic backscatter measurements near normal incidence, shadowing and multiple scattering effects are neglected.

The relief statistics of the sediment interface are assumed to be isotropic and described by Gaussian-distributed height deviations (ζ) about a mean plane, with rms height σ, and by a 2D energy density spectrum. Since ζ is usually not stationary, and since the choice of a reference surface is

Redistribution subject to ASA license or copyright; see http://acousticalsociety.org/content/terms. Download to IP: 132.177.229.80 On: Mon, 23 Nov 2015 20:45:01

somewhat arbitrary, it is useful to consider the height difference between points on the surface separated by a fixed distance (horizontal vector $\mathbf{r}$). This height difference is a locally stationary random variable whose mean-squared value is the structure function $D(\mathbf{r})$

$$D(\mathbf{r}) = \langle [\zeta(\mathbf{r}+\mathbf{r}_o) - \zeta(\mathbf{r}_o)]^2 \rangle. \tag{4}$$

As described in Appendix B of Ref. 21, the relief energy density spectrum $W(\mathbf{k})$ for the 2D spatial wave vector $\mathbf{k}$ of magnitude k, and the structure function are related by

$$D(\mathbf{r}) = 2\int_{-\infty}^{\infty}\int_{-\infty}^{\infty}(1-\cos(\mathbf{k}\cdot\mathbf{r}))W(\mathbf{k})d^2k. \tag{5}$$

Power-law relief spectra have been measured over a wide range of spatial wavelengths, from geographic scales (meters–kilometers)[22–24] to centimeter scales commensurate with high-frequency acoustic wavelengths.[25–28] The relief energy density spectrum $W(\mathbf{k})$ is formulated as[3,19]

$$W(\mathbf{k}) = w_2 k^{-\gamma}, \tag{6}$$

where the spectral strength w_2 has units of length to the power $(4-\gamma)$, whereas the spectral exponent γ is unitless. For a reference length h_o, $W(\mathbf{k}) = w_2(h_o k)^{-\gamma}$. This removes dimensionality from the power term, and gives w_2 the dimensionality of h_o^4. In this work $h_o = 1$ cm, and w_2 is expressed in cm^4.

Spectral analyses of centimeter-scale topography have yielded 2D spectral exponents in the range $2<\gamma<4$ (Refs. 25–28). In the absence of measurements, a mean value of $\gamma = 3.25$ can be assumed for most bottom types.[19] In practice, γ and w_2 are determined by straight-line regression fit to the 2D spectra plotted on log–log scale, over spatial wave numbers spanning roughly an order of magnitude above and below the acoustic wave number.

Integration of Eq. (5), after substituting in Eq. (6), yields a simple expression for the structure function[3]

$$D(r) = C_\zeta^2 r^{2\alpha}, \tag{7}$$

with the structure constant C_ζ given by

$$C_\zeta^2 = [2\pi w_2 \Gamma(2-\alpha)2^{-2\alpha}]/[\alpha(1-\alpha)\Gamma(1+\alpha)], \tag{8}$$

where Γ is the gamma function, and $\alpha = (\gamma/2) - 1$ is constrained between 0 and 1.

Following Jackson *et al.*,[3] the bandlimited power-law relief spectrum is separated into large- and small-scale roughness components with the boundary defined by a cutoff spatial wave number k_c

$$k_c = \left(\frac{\gamma-2}{8\pi w_2 k_a^2 \cos^2\theta_i}\right)^{1/(2-\gamma)}. \tag{9}$$

Within the bandlimited large-scale relief, we shall use also the mean-square slope ς^2 to compute sound energy transmission into the sediment, and the mean-square curvature R_c^{-2} for the Kirchhoff criterion

$$\varsigma^2 = 2\pi\int_0^{K_c} W(\mathbf{k})k^3 dk = \frac{2\pi w_2 k_c^{4-\gamma}}{4-\gamma}, \tag{10}$$

$$R_c^{-2} = 2\pi\int_0^{K_c} W(\mathbf{k})k^5 dk = \frac{2\pi w_2 k_c^{6-\gamma}}{6-\gamma}. \tag{11}$$

B. Sediment volume characteristics

At 10–100 kHz, penetration of water-saturated sediments is limited to the first several meters, and the bottom can be modeled as a lossy fluid with acoustic scattering due to fluctuations in the density and refraction indices of the medium. In addition, the intensity of a plane monochromatic sound wave entering the sediment is attenuated with distance. The corresponding attenuation coefficient α_b in dB/m is usually frequency dependent

$$\alpha_b = \kappa_p f_a^m, \tag{12}$$

where κ_p is an attenuation constant expressed in dB/m/kHz, and f_a is the acoustic frequency in kHz. For unconsolidated ocean sediments of the type presented here, we follow Hamilton's observations of $m=1$ and employ his regression equations[29] relating κ_p to the mean grain size (M_ϕ).

Ivakin and Lysanov[30] described a sediment volume backscatter model which includes the dissipative effects of a lossy medium and the transmission characteristics of a randomly rough interface. They used bottom slope variations to compute the energy transmitted through the interface. Jackson *et al.*[3] combined these ideas with Stockhausen's[31] scheme for subbottom acoustic scattering below a flat surface, by integrating transmission terms over a Gaussian distribution of incidence angles whose mean value was determined by the rms slope (ς). This approach is a variant of the composite roughness scattering model described by McDaniel and Gorman.[32] Here, we modify the composite roughness treatment to account for the finite duration of the transmitted signal.

C. Angle-dependent seafloor acoustic backscatter

Following the results of Jackson *et al.*,[3] the angular-dependent backscatter coefficient (s_i) at the water–sediment interface is given by

$$s_i(\theta_i) = \begin{cases} \mathcal{R}_\perp^2[8\pi\cos^2(\theta_i)\sin^2(\theta_i)]^{-1}\displaystyle\int_0^\infty \exp(-qu^{2\alpha}) \\ \quad \times J_o(u)u\,du & \theta_i > 0 \\ \mathcal{R}_\perp^2[8\pi\alpha]^{-1}C_\zeta^{-2/\alpha}(2k_a^2)^{(\alpha-1)/\alpha}\Gamma(1/\alpha) & \theta_i = 0, \end{cases} \tag{13}$$

with

$$q = \cos^2(\theta_i)\sin^{-2\alpha}(\theta_i)C_\zeta^2 2^{1-2\alpha}k_a^{2(1-\alpha)}. \tag{14}$$

In this formulation, J_o is the zeroth-order Bessel function of the first kind, and the normal incidence term is as derived in Ref. 4.

In the sediment volume, we use the unitless acoustic backscatter cross section per unit area per unit solid angle $s_{vl}(\theta_i)$, defined by

$$s_{vl}(\theta_i) = \sigma_2 \mathcal{V}_l(\theta_i)/\mathcal{A}, \quad \text{with } \mathcal{A} \equiv 2/(10\log_{10} e), \tag{15}$$

where $\mathcal{V}_l(\theta_i)$ accounts for the two-way transmission losses at the water–sediment interface with large-scale roughness hav-

Redistribution subject to ASA license or copyright; see http://acousticalsociety.org/content/terms. Download to IP: 132.177.229.80 On: Mon, 23 Nov 2015 20:45:01

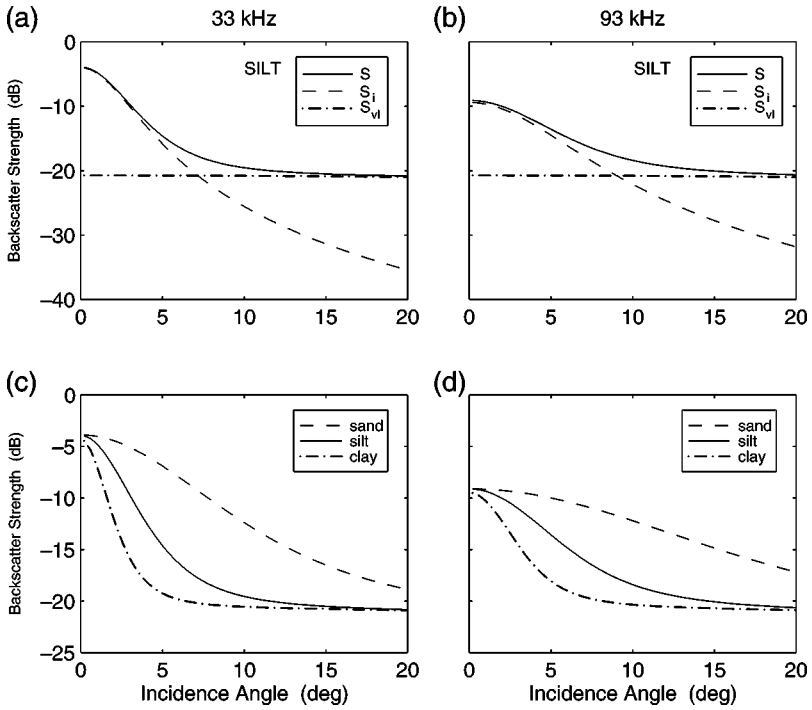

FIG. 2. Angular dependent seafloor acoustic backscatter at 33 and 93 kHz. Top row: total backscatter strength $S=10\log_{10}(s_i+s_{vl})$ over silt, and component backscatter strengths $S_i=10\log_{10}(s_i)$ for the interface term [Eq. (13)], and $S_{vl}=10\log_{10}(s_{vl})$ for the volume term [Eq. (15)]. Bottom row: total backscatter strength S over sand, silt, and clay.

ing small rms slope. This expression is identical to the large-scale volume scattering cross section described in Jackson *et al.*,[3] where $\sigma_2=\sigma_v/\alpha_b$ is termed the volume parameter, and σ_v is the volume scattering coefficient.

Stockhausen[31] gave an angle-dependent expression for two-way transmission through a flat water–sediment interface in terms of the plane-wave coherent reflection coefficient $\mathcal{R}$ and the sound-speed ratio ν at the interface

$$\mathcal{V}_f(\theta_i)=[1-\mathcal{R}^2(\theta_i)]^2\cos^2(\theta_i)[1-(\nu\sin(\theta_i))^2]^{-1/2}. \tag{16}$$

However, at 10–100 kHz very few water–sediment interfaces are likely to appear flat, and the effects of interface roughness must be considered in the two-way transmission through the interface. This is done by considering the distribution of incidence angles expected for large-scale roughness with local slope ϑ, such that the angle of incidence with respect to the local surface is $\theta_i-\vartheta$.

If we assume that the slopes are Gaussian distributed about the horizontal plane, with small rms slopes ($\varsigma<0.1$), then the transmission term for large-scale interface roughness, $\mathcal{V}_l$, is the average of the flat surface coherent reflection coefficients at each planar slope facet of the rough surface

$$\mathcal{V}_l(\theta_i)=\frac{1}{\sqrt{\pi}\varsigma}\int_{-(\pi/2-\theta_i)}^{\infty}\mathcal{V}_f(\theta_i-\vartheta)\exp\left(-\frac{\vartheta^2}{\varsigma^2}\right)d\vartheta. \tag{17}$$

Angle-dependent backscatter curves ($S(\theta_i)$) for sand ($M_\phi=2$), silt ($M_\phi=4$), and clay ($M_\phi=7$) substrates are computed for acoustic frequencies of 33 and 93 kHz, and plotted in Fig. 2, where generic values for the sediment geoacoustic parameters are correlated to mean grain size by the relationships described in Appendix A. These plots illustrate the dominance of interface scattering around normal incidence, giving way to volume scattering for angles exceeding 5–10 degrees. However, sand substrates exhibit a more gentle curve slope, whereas clay substrates exhibit large interface scattering strengths about normal incidence, falling off sharply as θ_i increases. As large particles are more likely than fines to settle in high-energy hydrodynamic environments, the relief energy density spectrum of coarse-grain sediments (small M_ϕ) typically has more energy (higher spectral strength w_2) than that of fine-grain sediments. An increase in w_2 causes a commensurate increase in the cutoff spatial wave number k_c [Eq. (9)]; hence, higher spatial frequencies are included in the theoretical large-scale surface roughness. It follows that the estimated rms slope (ς) of the interface increases, yielding more backscattered energy at higher angles and a backscatter curve with a gentler slope. While increasing roughness, relative to the acoustic wavelength, reduces the normal incidence component, this trend is typically offset by a commensurate rise in the impedance contrast ($\rho\nu$), resulting in $S(0)$ values which are similar for each of the three substrates.

D. Time-dependent sediment interface backscatter

Consider a monostatic transducer at altitude (a) which emits a pulse of duration τ_p seconds, with an intensity time series $I_x(t)$, $0\leqslant t\leqslant\tau_p$. The energy in the pulse propagates as a spherical shell with sound speed ν_w. The intersection of this shell with the bottom initially takes the shape of a disk, changing to that of an annulus. For a level surface, the pulse impacts nadir at time a/ν_w, and the annulus diverges from this point of origin. The bottom projection at some time $t>a/\nu_w+\tau_p$ is illustrated in Fig. 3.

The length of the pulse in water is $\nu_w\tau_p$, and its leading and trailing edges make angles θ_2 and θ_1, respectively, with nadir. The average echo intensity envelope $I_i(t)$ of the backscattered signal begins at the time of *bottom detect*, $t_{bd}=2a/\nu_w$. The backscattered energy in the scenario of Fig. 3

Redistribution subject to ASA license or copyright; see http://acousticalsociety.org/content/terms. Download to IP: 132.177.229.80 On: Mon, 23 Nov 2015 20:45:01

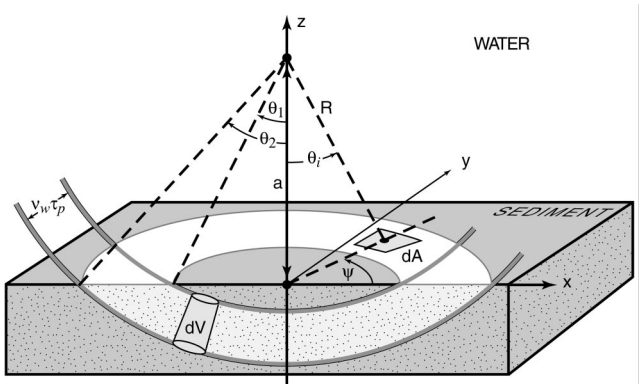

FIG. 3. Geometric representation of the elemental area dA and volume dV used to compute the time-dependent echo intensity envelope.

reaches the receiver at $t=t_{bd}/\cos\theta_2$. The elemental area dA is located at incidence angle θ_i, azimuthal angle ψ, and range $R=a/\cos(\theta_i)$ such that

$$dA=R^2\sin(\theta_i)d\theta_i\,d\psi. \tag{18}$$

Similar to sonar equation formulations described in Refs. 4, 11, 13, and 33, the total acoustic intensity field backscattered by the interface and received at the transducer is evaluated over the angular sectors $\theta_1\leqslant\theta_i\leqslant\theta_2$ and $0\leqslant\psi<2\pi$ by convolving the transmitted waveform $I_x(t)$ with the bottom backscattering coefficient $s_i(\theta_i)$ bound by the transducer beam pattern $b(\theta_i,\psi)$

$$I_i(t)=\int_{\psi=0}^{2\pi}\int_{\theta_i=\theta_1(t)}^{\theta_2(t)} I_x\left(t-\frac{2R}{\nu_w}\right)\frac{s_i(\theta_i)b^4(\theta_i,\psi)}{R^4 10^{\alpha_w R/5}}dA, \tag{19}$$

where

$$\theta_1(t)=\begin{cases}\cos^{-1}\left(\dfrac{2a}{\nu_w(t-\tau_p)}\right) & t-\tau_p\geqslant t_{bd}\\ 0 \quad t-\tau_p<t_{bd}\end{cases}$$

and (20)

$$\theta_2(t)=\begin{cases}\cos^{-1}\left(\dfrac{2a}{\nu_w t}\right) & t\geqslant t_{bd}\\ 0 \quad t<t_{bd},\end{cases}$$

and terms in the denominator of Eq. (19) account for spherical spreading and absorption in the water column during the round-trip travel of the pulse between the transducer and the seafloor. α_w is the frequency-dependent absorption coefficient in water. In the ideal case of a perfectly rectangular transmit pulse, the transmitted intensity $I_x(t-[2R/\nu_w])$ may be replaced by the constant I_x and moved outside the integral.

For sediment interface scattering we use the Kirchhoff approximation with the power-law roughness spectrum to calculate the bottom backscattering coefficient $s_i(\theta_i)$.[3,4,11] This approach has a frequency dependence based on power-law seafloor roughness spectra. This is in contrast to the geometrical optics approach which relies on the high-frequency limit of the Kirchhoff approximation, as described by Beckmann and Spizzichino[34] and Brekohvskikh and Lysanov,[35] and used in Pouliquen and Lurton[13] as a frequency-independent interface scattering component. This high-frequency limit does not exist in the power-law spectrum formulation chosen here. Although each approach has been used successfully in prior work,[7,11,13] we chose the frequency-dependent path because the power-law spectrum is linked to the relief statistics [Eq. (4)] of the types of sediments considered here.

Discrete formulation and implementation of our time-dependent sediment interface backscatter model is described in Appendix B 1.

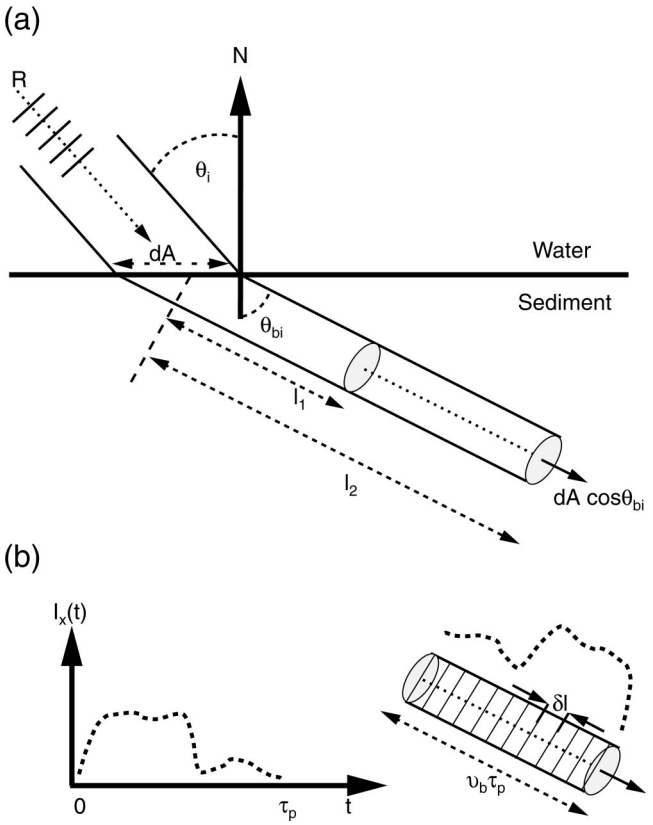

FIG. 4. Integration of backscattered energy from an elemental volume tube: (a) Volume scattering geometry, where scatterers within the tube are insonified from distances l_1 to l_2; (b) illustration of transmitted pulse and juxtaposition with region described in (a).

E. Time-dependent sediment volume backscatter

Single scattering is assumed and the statistics governing subbottom inhomogeneities are assumed to be isotropic and homogeneous, leading to a constant sediment volume scattering coefficient σ_v.

Figure 4(a) shows a closeup of the elemental surface dA at time $t>(R/\nu_w)+\tau_p$, where a portion of the incident energy has refracted into the sediment, and the edges of the pulse have propagation distances (l_1,l_2), referenced from the point of entry into the sediment.

We express the acoustic scattering from the sediment volume as a convolution of the transmit signal $I_x(t)$ with the volume scattering characteristics along the propagation path, taking into account the effects of transducer directivity and of round-trip spherical spreading and absorption in the water column. At time t, the total sediment volume backscattering

Redistribution subject to ASA license or copyright; see http://acousticalsociety.org/content/terms. Download to IP: 132.177.229.80 On: Mon, 23 Nov 2015 20:45:01

field $I_v(t)$ is the sum of all the contributions from volume tubes of cross section dA that converge at the transducer's face. It is expressed in integral form, over the angular intervals $0 \leqslant \theta_i \leqslant \theta_2$ and $0 \leqslant \psi < 2\pi$, as

$$I_v(t) = \int_{\psi=0}^{2\pi} \int_{\theta_i=0}^{\theta_2(t)} \frac{\sigma_v b^4(\theta_i,\psi)}{R^4 10^{\alpha_w R/5}} \mathcal{V}_l(\theta_i) \times \left\{ \int_{l_1(t)}^{l_2(t)} I_x\left(\tau_p - \frac{l - l_1(t)}{\nu_b} \right) e^{-2\beta_e l} dl \right\} dA, \quad (21)$$

with $\theta_2(t)$ defined in Eq. (20), and

$$l_1(t) = \begin{cases} \left[\frac{t}{2} - \tau_p - \frac{R}{\nu_w} \right] \nu_b & t \geqslant 2\left(\frac{R}{\nu_w} + \tau_p \right) \\ 0 & t < 2\left(\frac{R}{\nu_w} + \tau_p \right) \end{cases}$$

and (22)

$$l_2(t) = \begin{cases} \left[\frac{t}{2} - \frac{R}{\nu_w} \right] \nu_b & t \geqslant 2R/\nu_w \\ 0 & t < 2R/\nu_w . \end{cases}$$

Equation (21) is valid from normal incidence to the critical angle.

Spherical spreading within the elemental tubes is considered negligible, and the assumption of statistical volume homogeneity allows placement of σ_v outside the bracketed convolution integral. The integrand includes a spatial representation of $I_x(t)$, tempered by the absorption characteristics of the sediment. The round-trip attenuation between scattering center l and the water–sediment interface is expressed with the exponential intensity attenuation rate β_e, which has units of power nepers per unit distance.

In model computations, the transmitted waveform is digitized and the bracketed integrand of Eq. (21) is evaluated numerically at each time t. If one assumes a perfectly rectangular pulse, I_x may be moved outside of the integral, and the remaining expression evaluates to an attenuation length $L(t)$, which we define as

$$L(t) \equiv \int_{l_1(t)}^{l_2(t)} e^{-2\beta_e l} dl = \frac{1}{2\beta_e} (e^{-2\beta_e l_1(t)} - e^{-2\beta_e l_2(t)}). \quad (23)$$

Note that the time dependency can be removed by assuming an ideal rectangular pulse of length much greater than the energy extinction depth of the substrate, and by evaluating the integral for $l = [0,\infty]$. In this limiting case $L \approx 1/(\mathcal{A}\alpha_b)$, where $\alpha_b = 4.343\beta_e$ is the sediment compressional wave attenuation coefficient and $\mathcal{A} = 2/(10 \log_{10} e)$.

We follow Refs. 3, 4, and 11 and adopt Stockhausen's[31] semiempirical method for calculating the sediment volume backscatter coefficient σ_v (Sec. II C), employing two roughness scales for determining transmission of acoustic energy through the water–sediment interface,[3,4] instead of the physical approach of Chernov[36] and Ivakin and Lysanov,[30] based on estimates of sound speed and density fluctuations in the bottom, and used by Pouliquen and Lurton[13] with a flat water–sediment interface. Our conservative approach sacrifices sound speed and density heterogeniety inversion potential for straightforward estimates of seafloor volume scattering strength. We chose this simpler approach because volume heterogeneity measurements from undisturbed sediments are currently difficult to obtain,[37] and thus existing analytical descriptions of sound speed and density correlation lengths in the sediment are not yet validated. Eventually, the more stringent physical approach to estimating sediment volume characteristics should be a powerful addition to the inversion process.

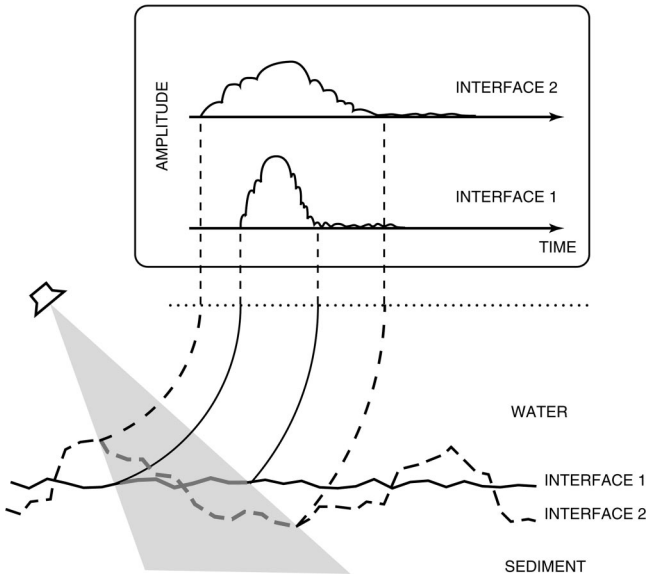

FIG. 5. Lengthening of the echo due to macro-roughness.

The discrete formulation of our time-dependent sediment volume backscatter model is described in Appendix B 2, with its implementation for finite duration, variable amplitude transmit signals.

F. Influence of seafloor macro-roughness

The model described so far predicts the average echo intensity envelope measured with a monostatic transducer aimed at the bottom. The model includes the ratio of scattered to incident energy as the pulse traverses the water–sediment interface and penetrates the substrate. Volume scattering is treated in three dimensions and scattering at the interface is essentially two-dimensional because the ensemble of scattering elements dA are aligned along a mean flat horizontal plane at distance a from the transducer (Fig. 3). Significant deviation of bottom relief from this mean plane at the scale of a beam footprint may result in elongation of the echo, as illustrated in Fig. 5. Temporal stretching of the echo due to large-scale bottom roughness is incorporated by convolving model computations based on the small-scale relief with the height distribution of the interface relief as described by several authors.[9,10,13,38,39] The specifics of our discrete implementation of this macro-roughness effect are described in Appendix B 4.

Redistribution subject to ASA license or copyright; see http://acousticalsociety.org/content/terms. Download to IP: 132.177.229.80 On: Mon, 23 Nov 2015 20:45:01

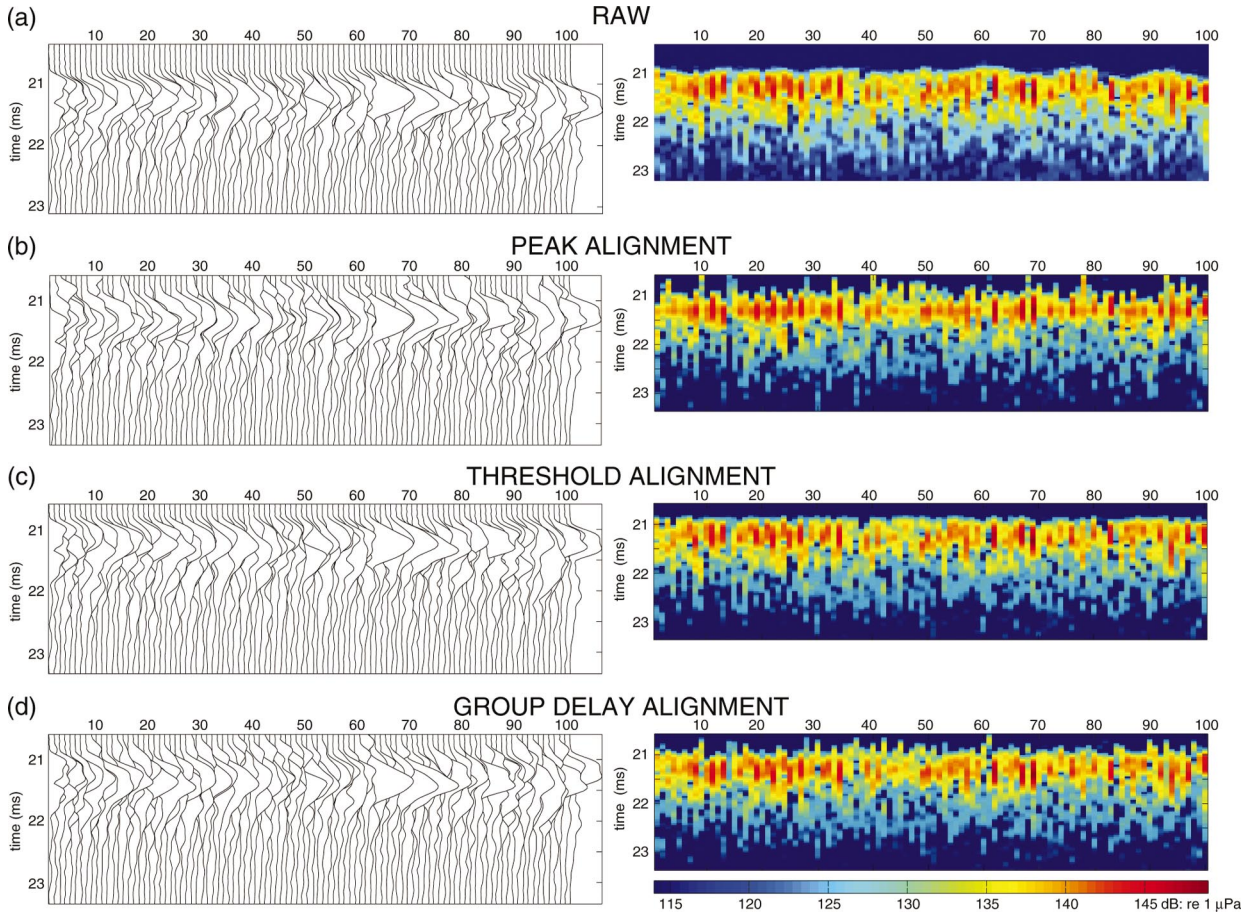

FIG. 6. Waterfall and raster plots illustrating the effect of echo alignment techniques: (a) none; (b) peak with horizontal red line at the signal maxima; (c) leading edge threshold; (d) group delay.

III. DATA

With a calibrated echo-sounder, bottom echoes were collected over substrates in San Diego Bay ranging from clay to sand. The acoustic frequencies (33 and 93 kHz), transducer orientations (maximum response axis at 0°–15° incidence), and −3-dB beamwidths (10°–21°) of the system are consistent with the scattering theory incorporated in the temporal model. The transducer was elevated to a specified angle from nadir in the roll plane. Angles of pitch and roll were digitized for each ping and, combined with knowledge of local bathymetry, used to determine the incidence angle (θ_T) of the transducer's maximum response axis.

The waterfall and raster plots of Fig. 6(a) depict 100 consecutive bottom echoes from the San Diego Bay silt substrate measured at 33 kHz, with $\theta_T = 2°$. With 5 pings per second at a vessel speed of 1 kn, a small bottom patch would typically be sampled 60 times over the −3-dB footprint of the beam; thus, spatial overlap of echoes between consecutive pings is greater than 98%.

Acoustic wavelengths at frequencies greater than 10 kHz are generally small compared to the large-scale relief of the water–sediment interface, resulting in mostly incoherent scattering of the incident acoustic energy [Eq. (1)]. As seen in Fig. 6(a), bottom echoes are incoherent, varying significantly in amplitude and shape as the sonar translates longitudinally above the interface. Because of this variability, echoes must be treated stochastically.

The measured bottom echo consists of a pulsed CW signal modulated by the scattering process. Envelope detection of this signal yields an rms pressure time series, $p(t)$, expressed in units of pascals (Pa), and represented by the discrete sequence $p[n]$ when sampled with a period τ_e. For comparison with the temporal model, an ensemble of M contiguous returns is characterized by the average echo sequence $p_a[n]$ with N samples, and a mean altitude ($\overline{a}$) representing the transducer–bottom distance along a vector normal to the water–sediment interface

$$p_a[n] = \frac{1}{M}\sum_{m=0}^{M-1} p[m,n], \quad n = 0,1,...,N-1. \tag{24}$$

As we only have knowledge of the signal at amplitudes above the noise floor, $p_a[n]$ is truncated at both ends by application of a threshold minimum, P_{th}. The leading edge index corresponding to P_{th} identifies the time of *bottom detect* (t_{bd}), allowing for calculation of the mean altitude

$$\overline{a} = \frac{v_w t_{bd}}{2}, \tag{25}$$

where straight-path association of $\overline{a}$ and t_{bd} is a reasonable assumption for the modest transducer elevation angles char-

Redistribution subject to ASA license or copyright; see http://acousticalsociety.org/content/terms. Download to IP: 132.177.229.80 On: Mon, 23 Nov 2015 20:45:01

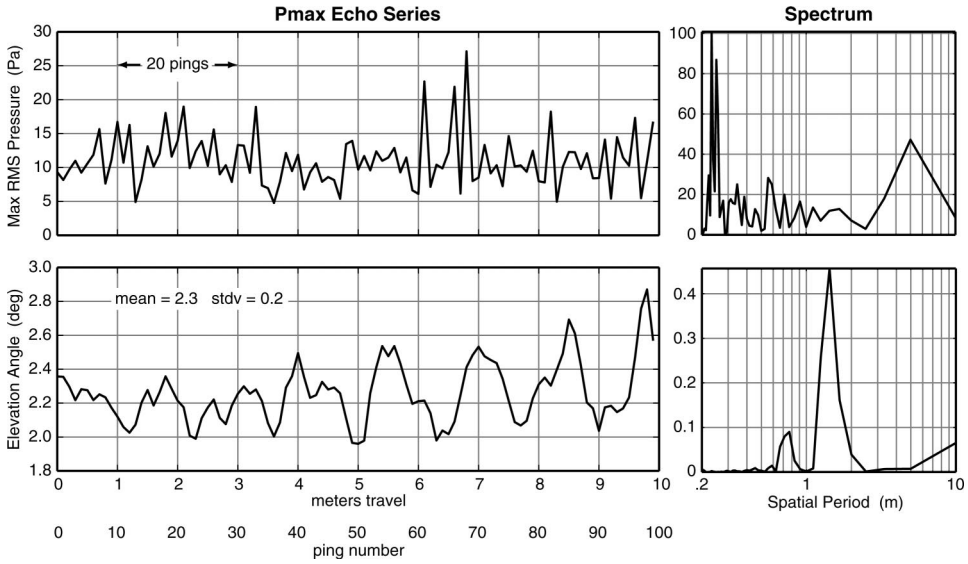

FIG. 7. Amplitude and spectra of peak rms pressure and corresponding transducer elevation angle measured along survey track.

acterizing the measurements. This value of $\overline{a}$ is used for generating the echo envelope model.

In the following sections the ensemble size (M) necessary for computing the average echo envelope is discussed, and alignment techniques compensating for vessel heave and topography variations are described.

A. Ensemble size

The left-hand-side plots of Fig. 7 represent the peak rms pressure (top) and the corresponding elevation angles measured with a clinometer for the 100 sequential echoes of Fig. 6(a). The energy density spectra displayed to the right indicate that most of the energy in the peak rms pressure sequence occurs at short spatial periods, and is minimal around 1.3 m—where the energy in the elevation angle spectrum is maximum. Hence, under stable survey conditions, changes in sensor attitude which are small relative to the beamwidth (standard deviation of 0.2° vs −3-dB beamwidth of 10°) have a negligible effect on the bottom echo statistics.

From analysis of a number of such data sets, we concluded that averaging over an echo ensemble covering the footprint of the −6-dB width of the beam (8.3 m in this scenario) provides adequate statistical representation. For the San Diego Bay measurements, $M=100$ pings meets or exceeds this criterion.

B. Echo envelope alignment

Envelope averaging should be performed on echoes that have been aligned in time, thus removing the effects of transducer heave and of small depth variations over consecutive pings. In this section, we compare the effectiveness of two common alignment techniques based on (1) the threshold minimum (P_{th}) and (2) the echo peak amplitude, and we introduce a third method which exploits phase information in the echo's discrete Fourier transform.

Echo alignment typically relies on tracking and indexing a temporal feature. The echoes within the ensemble are then shifted in time to line up on that feature. For the two-dimensional matrix $p[m,n]$ of Eq. (24), an alignment index (j_m) takes on integer values ($0 \leqslant j_m \leqslant N-1$). A mean alignment index, j, defined by

$$j = \frac{1}{M} \sum_{m=0}^{M-1} j_m , \tag{26}$$

leads to a delay $d_m = j_m - j$ for each of the M echoes. This yields the aligned array $p[m,(n-d_m)]$ that is substituted for $p[m,n]$ in (24) to compute the average echo sequence $p_a[n]$.

The temporal features presented here for comparison are labeled on the canonical echo envelope illustration of Fig. 8. This signal is characterized by a well-defined initial rise and peak amplitude, followed by a slow decay. The threshold minimum and peak amplitude indices associated with the times T_t and T_p are identified by serial search through the sequence, $p[n]$.

For echoes with poorly defined temporal features we employ T_g, which is determined by a process analogous to calculating the signal's group delay. This method provides an alignment index based on energy contributions spanning the entire length of the return, rather than on a single temporal

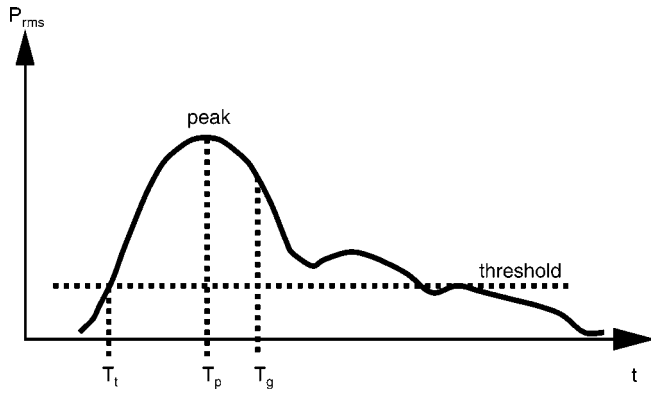

FIG. 8. Signal features used for echo envelope alignment offsets: threshold T_t (rising edge), T_p (peak), T_g (group delay).

Redistribution subject to ASA license or copyright; see http://acousticalsociety.org/content/terms. Download to IP: 132.177.229.80 On: Mon, 23 Nov 2015 20:45:01

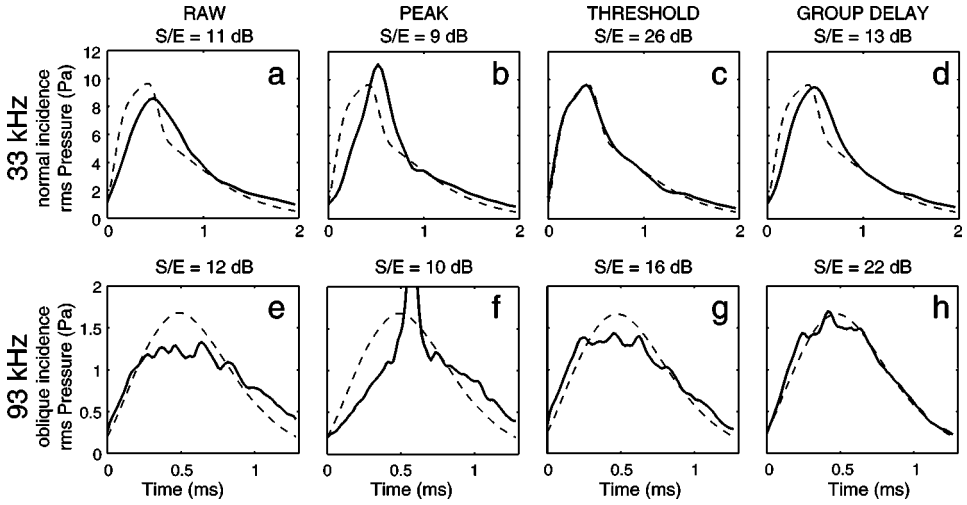

FIG. 9. Comparison of temporal model output (dashed line), given a silt substrate at normal incidence for 33 kHz, and at oblique incidence for 93 kHz, with stacked and averaged echoes (solid lines) for the various alignment techniques. From Sternlicht and de Moustier (Ref. 43).

feature. In this scheme, each sample of $p[n]$ is represented by a phasor $\mathcal{P}[n]$, with amplitude $p[n]$ and phase ϕ_n, such that

$$\mathcal{P}[n]=p[n]e^{i\phi_n}, \tag{27}$$

and

$$\phi_n=\frac{2\pi n}{N}-\pi, \quad -\pi\leqslant\phi_n<\pi. \tag{28}$$

The weighted phase ϕ for the energy in the echo envelope is determined by

$$\phi=\arg\left\{\sum_{n=0}^{N-1}\mathcal{P}[n]\right\}, \tag{29}$$

where ''arg'' refers to the phase of the bracketed quantity. Echoes situated near the beginning of the time window have a negative ϕ, whereas echoes situated toward the end of the window exhibit a positive ϕ. The alignment index (j_m) corresponding to the mth ping in an ensemble is calculated as

$$j_m=\frac{\phi+\pi}{2\pi}(N-1), \tag{30}$$

yielding $T_g=j_m\tau_e$. We refer to this method as group delay alignment, as expanding Eq. (29) reveals a formula similar to the phase slope of the discrete Fourier transform evaluated at the first two Fourier coefficients.

The effects of applying alignment techniques to an ensemble of measured echoes are illustrated in Figs. 6 and 9. The panels of Figs. 6(b)–(d) represent the adjusted envelopes $p[m,(n-d_m)]$ resulting from peak, threshold, and group delay alignments of the data in Fig. 6(a). In the top panels of Fig. 9, average echo envelopes created from these data segments are plotted alongside temporal model computations for which bottom characteristics were determined from grab samples and video images. The signal to error ratio (S/E) quantifies the model-data fits, and is evaluated as follows:

(1) Truncate the leading and trailing edges of the temporal model simulation, $\hat{p}_a[n]$, by applying the threshold minimum P_{th}.
(2) Align $p_a[n]$ and $\hat{p}_a[n]$ along their respective P_{th} leading edge indices.
(3) Truncate the tail end of the longer of the two time series such that $p_a[n]$ and $\hat{p}_a[n]$ are of equal length.
(4) Define n_1 and n_2 as initial and final indices for both waveforms and calculate S/E according to

$$\text{S/E}=\frac{\Sigma_{n=n_1}^{n_2}p_a^2[n]}{\Sigma_{n=n_1}^{n_2}(p_a[n]-\hat{p}_a[n])^2}, \tag{31}$$

for which a high value represents a ''good'' match of model with data.

This figure of merit is independent of signal scale and length, and thus provides a convenient comparison of matching results across data sets.

As seen in Fig. 9(a), averaging ''raw'' data may result in a distorted rising edge—quantified by the low S/E ratio of 11 dB. Alignment by peak tracking [Figs. 6(b), 9(b)] yields a poor representation of the echo. In general, alignments based on signal enhancement techniques (e.g., peak tracking and matched filters) induce vertical disproportions, unsuitable for echo envelope matching.

Bottom echoes from substrates whose relief is small compared to the acoustic wavelength exhibit consistent temporal energy distributions, particularly when measurements are conducted near normal incidence. In these situations, stacking and averaging via minimum threshold [Fig. 6(c)] preserves the integrity of the echo's rising edge, as demonstrated by the 26-dB signal to error match of Fig. 9(c).

In comparison to the other alignment techniques, group delay alignment [Fig. 6(d)] yields a more symmetric distribution of signal energy about the alignment index [Fig. 9(d)], and is less likely to trigger on an early blip or anomalous peak. Threshold alignment may be ineffectual in high-noise environments, or when signal shapes are highly variable—for example, when echoes are measured from substrates which are extremely rough relative to the acoustic wavelength. Under these conditions, group delay alignment may yield average echoes which are more consistent with theoretical predictions. This is illustrated by the 22-dB model–data match of Fig. 9(h), where the data were collected at 93 kHz and oblique incidence.

Based on the above, we have relied on threshold mini-

Redistribution subject to ASA license or copyright; see http://acousticalsociety.org/content/terms. Download to IP: 132.177.229.80 On: Mon, 23 Nov 2015 20:45:01

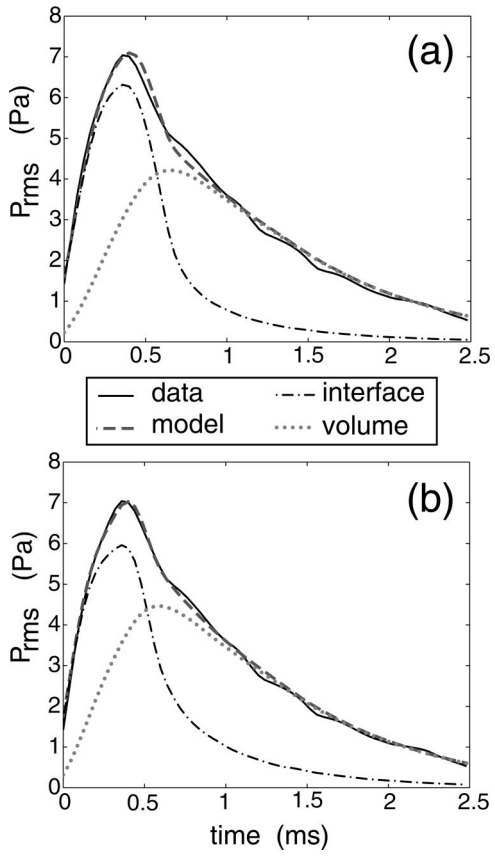

FIG. 10. Example of bottom type aliasing. 33 kHz data (solid line): San Diego Bay silt site. Model (dashed line): $\theta_T=8°$ and "optimum" parameter combinations: (a) "correct" solution: $M_\phi=4.76$, $\gamma=3.26$, $w_2=0.0012$, $\sigma_v=0.091$: S/E=27.6 dB. (b) "aliased" solution: $M_\phi=4.64$, $\gamma=3.00$, $w_2=0.0031$, $\sigma_v=0.111$: S/E=31.4 dB.

mum alignment for data with well-defined energy distributions and on group delay alignment otherwise.

IV. DATA–MODEL COMPARISON

Envelope detection, followed by the alignment and averaging steps described in Sec. III, yields an average rms pressure sequence, $p_a[n]$, whereas model computations yield an echo intensity. We chose to compare model and data as rms pressure sequences because the nonlinear conversion of the measured pressure signal in Pa to a power signal in W/m^2 introduced complications in the echo alignment procedures and in the matching operations. Therefore, a temporal model estimate $\hat{p}_a[n]$ is generated with specified mean altitude and sediment geoacoustic parameters

$$\hat{p}_a[n]=\sqrt{\rho_w \nu_w \hat{I}_a[n]}, \tag{32}$$

where $\hat{I}_a[n]$ represents the intensity of the computed echo envelope [Eq. (B8)] and ρ_w and ν_w correspond to seawater density and sound speed.

Figure 10 shows comparisons of model and averaged data for measurements at 33 kHz over a silt substrate. Henceforth, the sediment–water mass and density ratios (ρ,ν) and the sediment attenuation constant (κ_p) are correlated to the mean grain size parameter (M_ϕ) through the linear regression equations described in Appendix A. The interface contribution dominates the early part of the return, and volume contributions continue as the projection of the pulse exits the transducer beam footprint.

Panels (a) and (b) demonstrate two convincing matches, yet case (b) with the highest S/E represents an aliased solution, whereas the parameters inferred from (a) represent a closer match to those of a silt substrate. Accounting for ambiguous matches is a critical issue in using the model for parameter estimation. In the following sections we consider the influence of each parameter on the temporal model, and propose relief spectrum constraints consistent with ground-truth measurements. These constraints are used in a parameter estimation scheme described in the companion paper.[20]

A. Sensitivity of echo shape to model parameters

The influence of each parameter $(M_\phi,\gamma,w_2,\sigma_v)$ on echo shape is determined by comparing recorded data to iterations of the temporal model. We start in Fig. 11(c) with the closest match between the average echo from another set of 100 sequential echoes measured over a silt bottom, and a model echo with best-fit parameters yielding an S/E of 29.3 dB. Figure 11(d) illustrates the angular dependence curve for a substrate with these parameters: $S=10\log_{10}(s_i+s_{vl})$, where interface and volume scattering coefficients, s_i and s_{vl}, are described by Eqs. (13) and (15), respectively. All other parameters being held constant, each of the four parameters is increased [Figs. 11(a), (b)] or decreased [Figs. 11(e), (f)] relative to its best-fit value to evaluate its effect on the model output.

1. Grain size (Mϕ) influence on echo envelope

An increase in M_ϕ is accompanied by a lower signal amplitude [Fig. 11(a)]. This is due to the smaller impedance contrast $(\rho\nu)$, hence the lower backscatter strength (S), predicted for fine-grain sediments. The higher peak amplitude observed for lower M_ϕ is due primarily to higher impedance contrast [Fig. 11(e)]. The increase of energy in the *tail* of the backscattered signal seen in Fig. 11(a) is explained by the decrease in (κ_p) predicted for fine-grain, water-saturated sediments. These theoretical relationships are supported by the observation that bottom echoes from sand substrates typically exhibit large peak amplitudes (high reflection coefficients), whereas echoes from fine-grain sediments are characterized by long tails indicative of greater subbottom penetration.

2. Relief spectrum (γ,w_2) influence on echo envelope

Changes in either the spectral exponent γ or the spectral strength w_2 produce similar changes in the character of the backscattered echo. Their respective effects on the interface backscatter coefficient (s_i) depend on the range of spectral parameters considered. For the granular sediments studied in this work, the ranges likely to be encountered are $(3.0\leqslant\gamma\leqslant3.6)$ and $(0.0002\leqslant w_2\leqslant0.01)$. Within these boundaries, increasing γ or w_2 has the effect of increasing the cutoff spatial wave number k_c [Eq. (9)]; hence, higher spatial frequencies are included in the theoretical large-scale surface roughness. Likewise, the estimated rms slope (ς) of the bot-

Redistribution subject to ASA license or copyright; see http://acousticalsociety.org/content/terms. Download to IP: 132.177.229.80 On: Mon, 23 Nov 2015 20:45:01

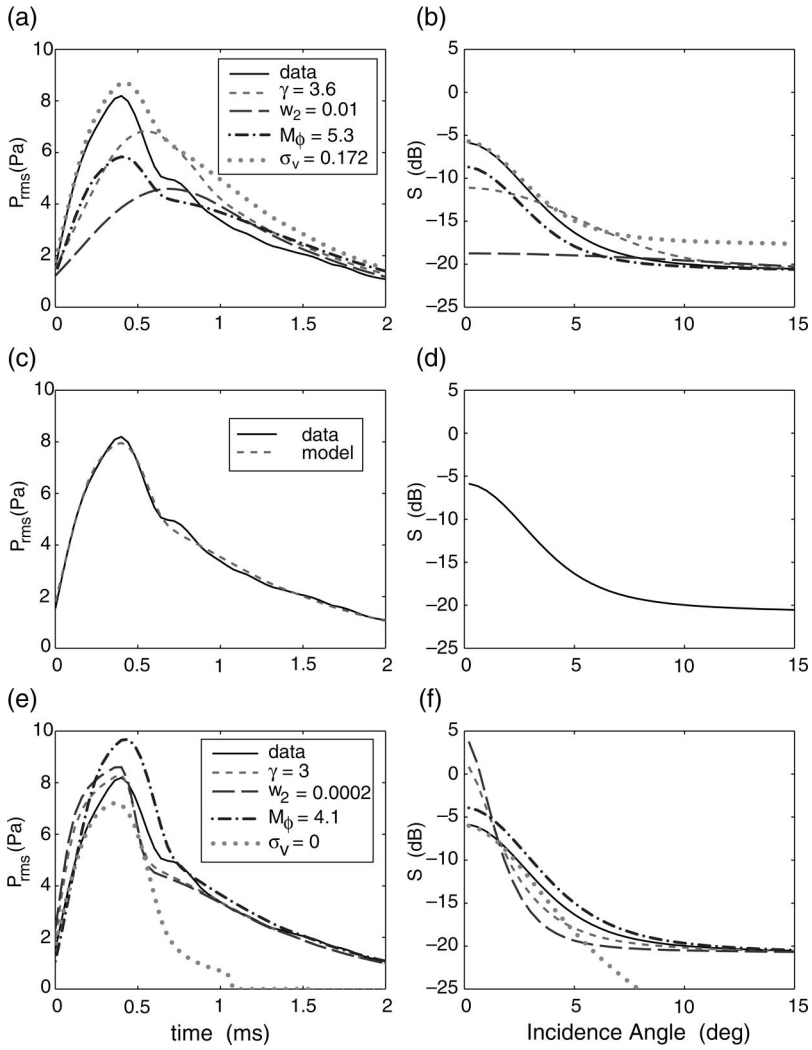

FIG. 11. Effects of geoacoustic parameters on modeled echoes. rms pressure envelopes and corresponding acoustic backscatter strengths (S) (data: solid line, model: dashed line). Best-fit model parameters for (c) and (d): $M_\phi = 4.68$, $\gamma = 3.3$, $w_2 = 0.0009\ \mathrm{cm}^4$, $\sigma_v = 0.086\ \mathrm{m}^{-1}$, $\theta_T = 8°$. (a), (b) and (e), (f) represent, respectively, increases ($M_\phi = 5.3$, $\gamma = 3.6$, $w_2 = 0.01\ \mathrm{cm}^4$, $\sigma_v = 0.172\ \mathrm{m}^{-1}$) and decreases ($M_\phi = 4.1$, $\gamma = 3.0$, $w_2 = 0.0002\ \mathrm{cm}^4$, $\sigma_v = 0\ \mathrm{m}^{-1}$) in the labeled geoacoustic properties, other parameters being held constant at the values in (c) and (d).

tom increases such that more energy is scattered at higher incidence angles, and proportionally less energy is scattered in the vicinity of the normal to the surface.

For higher values of γ or w_2 a gentler slope in the angular response is observed in Fig. 11(b), with a slow initial decay of backscatter strength from normal to higher incidence angles. Here, the backscatter strength at normal incidence is reduced, and there is a smaller dynamic range in levels between 0° and 15°. This is seen in the extreme for $w_2 = 0.01$, where the volume component dominates. Figure 11(a) shows that an increase in γ or w_2 lowers the peak amplitude of the bottom echo, and retards the rise and fall time of the interface scattering component, evidenced by the smearing of the original pulse shape. The shapes of these bottom echoes and angular response curves are characteristic of rough, hard substrates. However, the reduction in backscatter strength and peak echo amplitude observed in the theoretical plots of Figs. 11(a) and (b) are typically compensated by the large reflection coefficients characteristic of these substrates.

Decreased spectral exponent γ and spectral strength w_2 produce a steeper angular response near nadir, characterized by a fast initial decay of backscatter strength from normal to higher incidence angles [Figs. 11(e)–(f)]. The backscatter strength at normal incidence increases, and a large dynamic range is evident between 0° and 15°. The model envelopes of Fig. 11(e) show an increase in amplitude, and sharper rise and decay times.

3. Volume scattering (σ_v) influence on echo envelope

The contribution of subbottom scattering to the received echo is largely determined by the volume scattering coefficient σ_v, which affects energy levels in the tail of the signal. If σ_v is set to zero, the volume component of backscatter is absent. Once the bottom projection of the transmit pulse migrates out of the transducer's main beam, the signal amplitude becomes extremely small, as illustrated in Fig. 11(e). Doubling σ_v from its best-fit value yields a corresponding increase of 3 dB in P_{rms} and S [Figs. 11(a)–(b)].

B. Ambiguities—relief spectrum constraints

The echo envelope model presented here is a function of measurable bottom characteristics, and may be used to predict echo shapes and amplitudes from well-characterized sediments. However, a more useful (and more difficult) application is that of fitting the model to data for sediment classification purposes; that is, extracting parameter combinations which are meaningful, unique, and most importantly,

Redistribution subject to ASA license or copyright; see http://acousticalsociety.org/content/terms. Download to IP: 132.177.229.80 On: Mon, 23 Nov 2015 20:45:01

TABLE I. Published 2D relief spectrum parameters. Comments: ACS=Anisotropic Across-Strike, AAS =Anisotropic Along-Strike. Notation: ~ estimated value, ⇀ graphics offset.

Substrate	Mean grain size (PHI)	Spectral exponent γ	Spectral strength w_2 (cm^4)	Source (Ref. no.)	Comments	Symbol
Coarse sand	0.2~	3.05	0.000 27	26		○
Coarse sand	0.5	2.47	0.006 54	41	Shell hash	
Coarse sand	0.5~	3.46	0.004 73	26	ACS storm gen ripples	○
Coarse sand	0.8	3.12	0.008 49	28	Shell hash	○
Medium sand	1.0	3.0	0.004	25	Shell Fragments	○
Medium sand	1.5~	3.29	0.000 46	26	ACS	○
Medium sand	1.5~	2.33	0.000 38	26	AAS	
Fine sand	2.0	3.0	0.003	25		○
Fine sand	2.5	2.92	0.006 16	42		○
Fine sand	2.5~	3.72	0.000 43	26	Sand dollar smoothing	
Fine sand	2.75~	3.17	0.005 55	26		○
Fine sand	3.0~	3.50	0.000 81	26		○
Very fine sand	3.0	3.3	0.174	25	Dense live shellfish	
Very fine sand	3.0	3.67	0.004 22	26	ACS	
Very fine sand	3.0	3.92	0.005 98	26	AAS	
Silty sand	4.8	3.5	0.004 6	25		*
Mud	5.5	3.18	0.003 18	26	Bimodal clay/sand-gravel	*
Silt	6.4	3.65	0.000 846	27	Prestorm	*
Silt	6.4	3.73	0.000 826	27	AAS poststorm	
Silt	6.4	3.38	0.000 912	27	Prestorm	*⇀6.6
Silt	6.4	3.56	0.001 296	27	ACS poststorm	
Sand–silt–clay	6.5	3.29	0.012 2	28		
Silty clay	9.9	3.42	0.002 31	28	Methane bubbles	*

correct. Unambiguous identification of a best fit is optimized when each of the fitting parameters has a unique effect on the model's output.

To first order, the grain size parameter (M_ϕ) controls the simulated echo's peak amplitude, whereas the volume parameter (σ_v) controls the energy in the signal's tail. The roughness parameters, γ and w_2, control the width and rise time of the signal's peak, but do so in similar fashion as discussed in Sec. IV A 2. The competing effects of these two parameters may lead to several solutions which qualify as ''good'' model–data fits.

Relief spectrum parameters derived from model–data comparisons using four-parameter ($M_\phi, \gamma, w_2, \sigma_v$) unconstrained global model–data optimization techniques (described in Ref. 20) produced substantially different (γ, w_2) combinations. This situation is illustrated by the model–data comparisons of Fig. 10, in which the better fit [Fig. 10(b)] represents a misleading solution according to criteria established below.

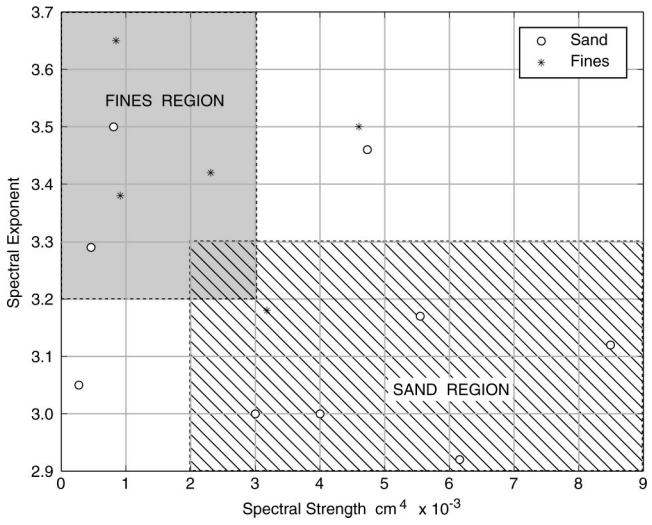

FIG. 12. Published relief spectrum parameters: γ vs w_2 (Table I).

For insight into how relief spectrum parameters relate to bottom type, published relief spectra are summarized in Table I. Measured spectral parameters are listed by bottom type in order of increasing M_ϕ, and a vertical space separates ''sands'' from ''fines.'' The 1D relief spectrum is published in many of the references; the 2D analogs listed are calculated using assumptions of isotropy.[19] Inspection of the table shows the large diversity of spectral parameters measured for sands and fine-grain sediments. To identify trends in the direct roughness measurements, a scatter plot of (γ vs w_2) for the published spectra is presented in Fig. 12. Plots illustrating how γ and w_2 vary with grain size (M_ϕ) are presented in Fig. 13.

Ignoring outliers and redundant measurements, the data in these graphs are a subset of the values listed in Table I—distinguished by the sand symbols (○) and fines symbols (*) listed in the far right column. The shaded γ and w_2 regions (Figs. 12,13) are those which we infer to be characteristic of sand and silts, with boundaries specified in Table II. This grouping of spectral parameters makes physical sense. Large particles are more likely than fines to settle in high-energy environments; hence, sand substrates should exhibit more energy at lower spatial wavelengths (i.e., higher w_2) than their fine-grain counterparts.

Redistribution subject to ASA license or copyright; see http://acousticalsociety.org/content/terms. Download to IP: 132.177.229.80 On: Mon, 23 Nov 2015 20:45:01

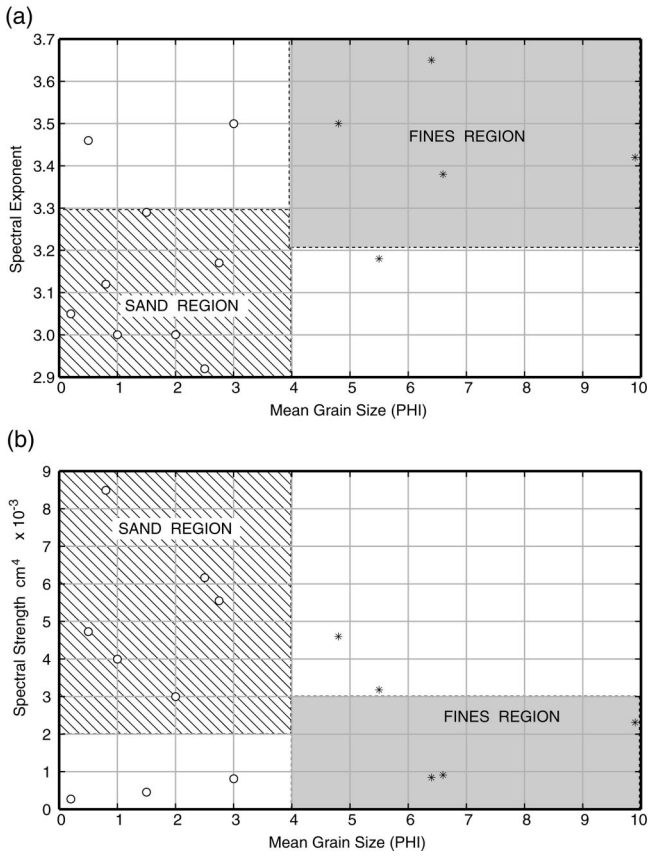

FIG. 13. Published relief spectrum parameters: γ and w_2 vs M_ϕ (Table I).

The exceptions to this rule are disconcerting and warrant closer examination. As evident in Fig. 13, a progressive reversal of the spectral parameters takes place and is most clearly observed for $(M_\phi = 2.5, 2.75, 3.0)$, where large γ values are associated with small w_2 values and, conversely, large w_2 values are associated with small γ values. In Fig. 14, the 2D relief spectra for these three grain sizes are plotted in log–log scale to demonstrate the potential for ambiguities in the linear representation of the power-law relief spectrum, where the spectral ''slope'' is equal to γ, and w_2 represents the energy at the intercept $(k=1)$.

For the relief spectrum parameters (γ, w_2) reported in the literature (Table I): first, the 1D spectra of an ensemble of fine-scale bottom profiles are averaged; the 1D slope and intercept of the average spectrum is determined through linear regression; then, assuming bottom isotropy, the 1D spectral parameters are converted to 2D spectral parameters. The average spectra can be quite noisy, as illustrated by relief spectrum plots presented by Briggs,[26] so a degree of ambiguity is likely in these estimates, which may explain the wide range of spectral parameters reported in the literature. We have observed similar ambiguities in unconstrained optimization of model parameters from our acoustic data, which

TABLE II. Relief spectrum boundaries for granular substrates.

Substrate	M_ϕ	γ	w_2 (cm^4)
Sand	$M_\phi < 4$	$\gamma < 3.3$	$w_2 > 0.002$
Fines	$M_\phi > 4$	$\gamma > 3.2$	$w_2 < 0.003$

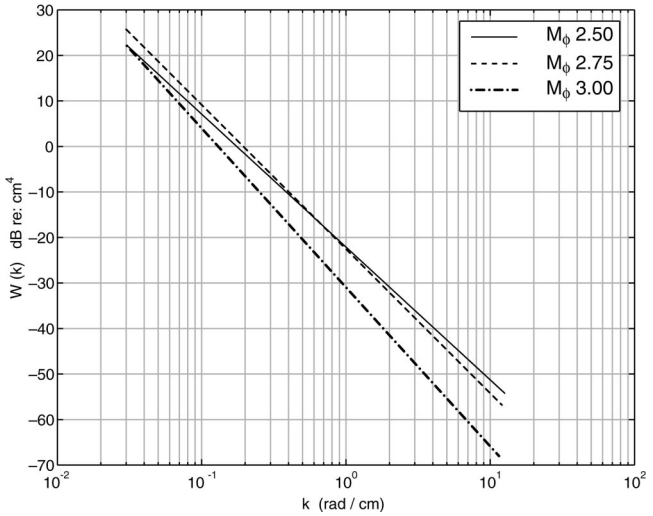

FIG. 14. Relief spectra plots for published parameters derived from topographic data.

suggests that spectral parameter estimates from topographic and acoustic data share similar degrees of uncertainty.[40]

For the San Diego Bay data that we have collected and processed, fewer ambiguous results were obtained when the (γ, w_2) constraints proposed in Table II were enforced during four-parameter model–data matching procedures. This led to the development of a two-stage optimization procedure where for the first stage γ is set to 3.25, the generic value[19] which falls conveniently within the overlap of the regions proposed for sand and fines. For the second stage, γ is set to a value dependent on the initial estimate of mean grain size, $\hat{M}_\phi$. Model–data matching tests using γ constants within the proposed boundaries led us to replace Table II with the simple rule

If $M_\phi < 4.0 \quad \gamma = 3.0$,

If $M_\phi \geqslant 4.0 \quad \gamma = 3.3$.

Subsequently global optimizations were carried out over (M_ϕ, w_2, σ_v), resulting in convergence to unique and sensible solutions.[20]

V. SUMMARY AND CONCLUSIONS

A time-dependent model of the acoustic intensity backscattered by the seafloor was described and compared with data from a calibrated, vertically oriented, echo-sounder operating at 33 and 93 kHz. The model incorporates the characteristics and geometry of the echo-sounder: the transducer's beam pattern, altitude off the bottom, tilt with respect to vertical, and the characteristics of the transmitted sound pulse; and environmental factors: spherical spreading and absorption losses, backscattering of the signal at the water–sediment interface, and by inhomogeneities in the sediment volume.

Scattering from the interface is predicted using Helmholtz–Kirchhoff theory, with physical parameters consisting of the strength (w_2) and exponent (γ) of a power law defining the 2D interface roughness spectrum, the ratio of sediment saturated bulk density over water mass density (ρ),

Redistribution subject to ASA license or copyright; see http://acousticalsociety.org/content/terms. Download to IP: 132.177.229.80 On: Mon, 23 Nov 2015 20:45:01

and the ratio of sediment sound speed over water sound speed (ν). A modified version of the composite roughness model, accounting for the finite duration of the transmitted signal, predicts the energy backscattered from the sediment volume. This contribution to the measured intensity field is determined by the subbottom's volume scattering and attenuation coefficients (σ_v and κ_p, respectively), as well as the water–sediment interface characteristics governing sound transmission into the sediment. Temporal stretching of the echo due to large-scale bottom roughness is incorporated by convolving model computations with the height distribution of the interface relief.

Envelope averaging is performed on echoes aligned in time, where alignments along threshold minima are applied to data with well-defined energy distributions, and offsets calculated from the phase slope of the envelope spectra are applied otherwise. The resulting rms pressure of the measured backscattered signal is compared with estimates of echo intensity converted to pressure [Eq. (31)]. Favorable comparisons of model and data were achieved by correlating the acoustic impedance and attenuation properties of the bottom with measures of its mean grain size (M_ϕ). Estimation of parameters ($M_\phi, \gamma, w_2, \sigma_v$) from fitting the model to data reveal ambiguous ranges for the two spectral parameters. However, analyses of model outputs and of physical measurements reported in the literature yield practical constraints on the roughness spectrum parameters. These constraints are used to estimate geoacoustic parameters through an optimized echo envelope matching techinque described in a companion paper.[20]

A. Limitations

The echo envelope model assumes isotropic and Gaussian-distributed bottom relief, sediment homogeneity in the upper few meters, as well as sediment–water impedance ratios ($\rho\nu$), and sediment acoustic attenuation constants (κ_p) consistent with mean empirical measures. Radical departure from these conditions may invalidate model results. Bottom samples and video images indicated that the sediments surveyed in San Diego Bay generally met these standards. However, model computations may not produce reliable results for complicated biogenic or anisotropic sediments.

Limitations on interface curvature dictated by the Kirchhoff approximation also restrict modeling to sediments having a large rms radius of curvature relative to the acoustic wavelength. This excludes extremely rough (rocky) substrates, or operation at high frequencies (>100 kHz). To evaluate the usefulness of the temporal model for characterizing a broader range of substrates, measurements at a variety of well-characterized sites will be necessary.

ACKNOWLEDGMENTS

We are grateful to the Space and Naval Warfare Systems Center (SPAWAR) for their assistance in collecting acoustic data and bottom samples, Reson Inc. for the generous loan of sonar transducers, and ORINCON Defense for their professional support. We thank Darrell Jackson for his input during the course of this research, and Jo Griffith for her help in preparing the illustrations. This work was funded by the Office of Naval Research under Contract No. N00014-94-1-0121.

APPENDIX A: GENERIC VALUES FOR GEOACOUSTIC MODEL PARAMETERS

The equations used in this work relating geoacoustic model parameters to particle size distribution ($-1 \leqslant M_\phi \leqslant 9$) are adapted from the APL-UW High-Frequency Ocean Environmental Acoustics Models Handbook.[19] The difference between our equations and Ref. 19 is that, in place of the volume parameter (σ_2), we establish a separate particle size mapping to the volume scattering coefficient (σ_v)

$$\begin{aligned}
\rho &\equiv \frac{\rho_b}{\rho_w} \\
&= 0.007\,797\ M_\phi^2 - 0.170\,57\ M_\phi + 2.3139, && -1 \leqslant M_\phi < 1 \\
&= -0.016\,540\,6\ M_\phi^3 + 0.229\,020\,1\ M_\phi^2 - 1.106\,903\,1\ M_\phi \\
&\quad + 3.0455, && 1 \leqslant M_\phi < 5.3 \\
&= -0.001\,297\,3\ M_\phi + 1.1565, && 5.3 \leqslant M_\phi \leqslant 9
\end{aligned} \tag{A1}$$

$$\begin{aligned}
\nu &\equiv \frac{\nu_b}{\nu_w} \\
&= 0.002\,709\ M_\phi^2 - 0.056\,452\ M_\phi + 1.2788, && -1 \leqslant M_\phi < 1 \\
&= -0.001\,488\,1\ M_\phi^3 + 0.021\,393\,7\ M_\phi^2 - 0.138\,279\,8\ M_\phi \\
&\quad + 1.3425, && 1 \leqslant M_\phi < 5.3 \\
&= -0.002\,432\,4\ M_\phi + 1.0019, && 5.3 \leqslant M_\phi \leqslant 9
\end{aligned} \tag{A2}$$

$$\gamma = 3.25, \qquad -1 \leqslant M_\phi \leqslant 9 \tag{A3}$$

$$\begin{aligned}
w_2 &= 0.002\,07\left(\frac{2.038\,46 - 0.269\,23\ M_\phi}{1.0 + 0.076\,923\ M_\phi}\right)^2, && -1 \leqslant M_\phi < 5.0 \\
&= 0.000\,517\,5, && 5.0 \leqslant M_\phi < 9.0
\end{aligned} \tag{A4}$$

$$\begin{aligned}
\kappa_p &= 0.4556, && -1 \leqslant M_\phi < 0 \\
&= 0.0245\ M_\phi + 0.4556, && 0 \leqslant M_\phi < 2.6 \\
&= 0.1245\ M_\phi + 0.1978, && 2.10 \leqslant M_\phi < 4.5 \\
&= 0.200\,98\ M_\phi^2 - 2.5228\ M_\phi + 8.0399, && 4.5 \leqslant M_\phi < 6.0 \\
&= 0.0117\ M_\phi^2 - 0.2041\ M_\phi + 0.9431, && 6.0 \leqslant M_\phi < 9.5 \\
&= 0.0601, && 9.5 \leqslant M_\phi
\end{aligned} \tag{A5}$$

$$\sigma_v = 0.004\alpha_b, \qquad -1 \leqslant M_\phi \leqslant 9. \tag{A6}$$

Redistribution subject to ASA license or copyright; see http://acousticalsociety.org/content/terms. Download to IP: 132.177.229.80 On: Mon, 23 Nov 2015 20:45:01

APPENDIX B: IMPLEMENTATION OF TIME DEPENDENT BACKSCATTER

1. Sediment interface backscatter

Equation (19) is computed numerically using a discrete representation in which the received signal is calculated at intervals of τ_s seconds and indexed by n such that $t=n\tau_s$. Isotropy is assumed in order to reduce the two-dimensional surface integral to a one-dimensional function of the angle of incidence θ_i. Then, the seafloor may be divided into a series of J concentric annuli, with indices j. The area $A[j]$ of each annulus, with range $R[j]=a/\cos(\theta_{ij})$ to its geometric center and radii $r_1[j]$ and $r_2[j]$, is calculated by

$$A[j]=\pi(r_2^2[j]-r_1^2[j]). \tag{B1}$$

Formulation of $r_1[j]$ and $r_2[j]$ depends on the strategy used to partition the insonified area. The indexed angles θ_{ij} may have equal increments in θ_i or they may be calculated via equal increments in the ring radius, r. The former paradigm is used here because it provides finer angular resolution close to normal incidence.

If the change in range from the near to the far edge of $A[j]$ is sufficiently small compared to the length of the pulse, the energy received from $A[j]$ at time index n can be expressed in a form similar to the integrand of Eq. (19) and summed over the elemental annuli, bound by indices $j_1[n] \leqslant j \leqslant j_2[n]$, which overlap the leading and trailing edges of the pulse projection at time index n

$$I_i[n]=\sum_{j=j_1[n]}^{j_2[n]} I_x\left(n\tau_s-\frac{2R[j]}{\nu_w}\right)\frac{s_i[j]A[j]}{att[j]}\mathcal{B}_m[j], \tag{B2}$$

where $s_i[j]$ is the backscatter coefficient, $att[j]$ accounts for the transmission loss in the water column

$$att[j]=R^4[j]10^{\alpha_w(R[j])/5}, \tag{B3}$$

and $\mathcal{B}_m[j]$ is the discrete implementation of the mean directivity function $\mathcal{B}_m(\theta_i)$

$$\mathcal{B}_m(\theta_i)=\frac{1}{2\pi}\int_0^{2\pi} b^4(\theta_i,\psi)d\psi. \tag{B4}$$

When the transmit waveform is represented by a sampled sequence $I_x(n\tau_s)$, the value of $I(n\tau_s-[(2R[j])/\nu_w])$ may be determined by interpolation or rounding.

2. Sediment volume backscatter

The discrete representation of Eq. (21) that we use for numerical computations requires an array for the volume tube [Fig. 4(b)]. An M element array of penetration lengths l_m defines volume cell centers, where l_1 represents the cell at the surface, and l_M the cell at the substrate's *skin depth*, d_s, that we define as the depth at which the signal strength drops by 10 dB

$$d_s=\frac{10+10\log_{10}(1-\mathcal{R}_{\min}^2)}{\alpha_b}, \tag{B5}$$

where for a specific sediment type, $\mathcal{R}_{\min}$ is the minimum angle-dependent reflection coefficient. The width of each cell, δl, is chosen to reflect the resolution of the time-sampled transmit pulse. Here, we chose $\delta l=\nu_b\tau_s/2$, which corresponds to the round-trip path length of the signal, per sample period.

Insonification of the volume continues for some time after the trailing edge of the pulse has passed over the surface patch. Thus, within practical constraints dictated by the skin depth, sediment volume contributions $I_v[n]$ are calculated between nadir ($j=1$) and the annulus overlapping the leading edge ($j=j_2[m]$)

$$I_v[n]=\sum_{j=1}^{j_2[n]}\left(\frac{\sigma_v\mathcal{B}_m[j]}{att[j]}\mathcal{V}_l[j]A[j] \times \sum_{m=m_1[j,n]}^{m_2[j,n]} I_x\left(\tau_p-\frac{l_m-l_{m_1[j,n]}}{\nu_b}\right)L[m]\right), \tag{B6}$$

where $m_2[j,n]$ and $m_1[j,n]$ index the volume cells which overlap the leading and trailing edges of the pulse at $n\tau_s/2$. As before, when the transmit waveform is represented by a sampled time series $I_x(n\tau_s)$, the value of $I_x(\tau_p-[(l_m-l_{m_1[j,n]})/\nu_b])$ may be determined by interpolation or rounding. This function is defined solely within the interval for which the pulse insonifies the volume annulus j bound by the surface and propagation length d_s.

The attenuation length $L[m]$ [the discrete version of Eq. (23)], is an array with elements

$$L[m]=\frac{1}{\mathcal{A}\alpha_b}(e^{-\mathcal{A}\alpha_b(l_m-\delta l/2)}-e^{-\mathcal{A}\alpha_b(l_m+\delta l/2)}), \quad 1\leqslant m\leqslant M. \tag{B7}$$

3. Echo signal intensity

The pressure contributions to the total field that are backscattered by the water–sediment interface and by sub-bottom volume inhomogeneities are assumed to be uncorrelated, and the total intensity received at time $n\tau$ is expressed with a simple addition of these contributions

$$I[n]=I_i[n]+I_v[n], \tag{B8}$$

where for large-scale roughness, $I_i[n]$ is computed with Eq. (B2) and $I_v[n]$ is computed with Eq. (B6).

4. Seafloor macro-roughness

Like Berry and Blackwell,[9] Haines and Langston,[10] Ogilvy,[38,39] and Pouliquen and Lurton,[13] we account for seafloor macro-roughness by convolving the ''smooth surface'' response with a roughness response. Within the length r_f of the footprint of the -3-dB width of the beam pattern along the interface, the macro-roughness corresponds to an altitude change ζ about a plane at mean altitude $\bar{a}$ such that $(\zeta=a-\bar{a})$ is a zero-mean Gaussian random variable with variance σ_a^2. Assuming that a power-law relief spectrum is valid for the macro-roughness at length scales of order r_f, such that mean-square height differences across the footprint increase with increasing footprint size, a measure of σ_a^2 is given by the structure function [Eq. (4)] evaluated at r_f

$$\sigma_a^2=C_\zeta^2 r_f^{2\alpha}. \tag{B9}$$

Redistribution subject to ASA license or copyright; see http://acousticalsociety.org/content/terms. Download to IP: 132.177.229.80 On: Mon, 23 Nov 2015 20:45:01

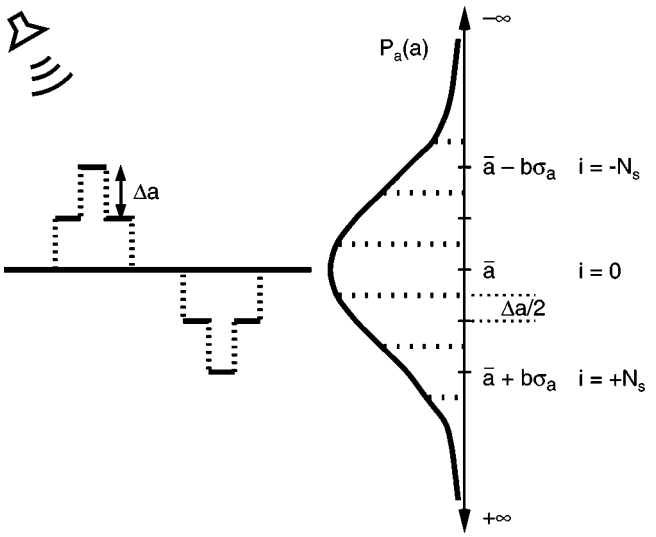

FIG. 15. Probability density function of altitude associated with macro-roughness. The independent axis of the altitude PDF $\mathcal{P}_a(a)$ is oriented along the vertical.

As illustrated in Fig. 15, for numerical computations, we must specify a finite range of altitudes about the mean plane $\overline{a}$ over which the macro-roughness is considered, and then normalize the corresponding area under the altitude probability density function $\mathcal{P}_a(a)$ to 1 in order to retain the total signal energy.

For each seafloor altitude index *i*, illustrated in Fig. 15, a suitably delayed echo is computed and weighted by the probability mass function $\mathcal{P}_a[i]$, which is derived from the Gaussian function illustrated on the right side of the figure. Convolution of the temporal model with this altitude distribution is achieved by summation along the indices of these delayed and weighted model outputs.

For a given angle of incidence θ_o at bottom detect time, discrete altitude increments Δa are computed at the sampling period τ_s

$$\Delta a = \nu_w \tau_s \cos(\theta_o)/2, \tag{B10}$$

and we sum over (N_s) increments above and below the mean plane $\overline{a}$

$$N_s = \mathrm{int}[b\sigma_a/\Delta a], \tag{B11}$$

where b is a fractional constant specifying the percentage of the distribution included in the computation, and ''int'' signifies rounding to the nearest integer value. We use an empirically derived $b=1.28$ (specifying 80% of the distribution) for fine-grain sediments (muds), and $b=0.5$ (40% of the distribution) for coarse-grain sediments (sand). The discrete implementation of the effects of macro-roughness is then expressed as

$$I_m[n] = \begin{cases} \sum_{-N_s}^{N[n]} I[n\tau_s - i\tau_s, a_s[i]]\mathcal{P}_a[i] & n \geqslant (\overline{a} - b\sigma_a)/\Delta a \\ 0 & \text{otherwise,} \end{cases} \tag{B12}$$

where $a_s[i] = \overline{a} + i\Delta a$ represents the height for model index *i*

$$N[n] = \begin{cases} n - \overline{a}/\Delta a & (\overline{a} - b\sigma_a)/\Delta a \leqslant n \leqslant (\overline{a} + b\sigma_a)/\Delta a \\ N_s & n > (\overline{a} + b\sigma_a)/\Delta a, \end{cases} \tag{B13}$$

and the discrete probability mass function $\mathcal{P}_a[i]$ is calculated by integrating the normal distribution between $(\xi_1 = a_s[i] - \Delta a/2)$ and $(\xi_2 = a_s[i] + \Delta a/2)$ such that

$$\mathcal{P}_a[i] = \Phi\left(\frac{\xi_2 - \overline{a}}{\sigma_a}\right) - \Phi\left(\frac{\xi_1 - \overline{a}}{\sigma_a}\right), \tag{B14}$$

where Φ is the distribution function of a normal random variable. For conservation of energy, $\mathcal{P}_a[i]$ must be normalized to 1, such that

$$\mathcal{P}_a[i] = \mathcal{P}_a[i] + \frac{1 - \Sigma_{-N_s}^{N_s} \mathcal{P}_a[i]}{2N_s + 1}. \tag{B15}$$

Macro-roughness lengthens the rise and decay times of the echo envelope and it reduces the maximum signal strength. In the model, these distortive effects are expected to be more pronounced for sand substrates whose macro-roughness standard deviation σ_a is predicted to be about three times as large as that of clay (11.5 cm vs 4.4 cm). A weakness of this approach is that when comparing the model with data, differing values of the macro-roughness parameter (b) are required for sand and fine-grain sediments. For unambiguous estimates of sediment characteristics from bottom echo envelopes, a more sophisticated approach to modeling the effects of macro-roughness will eventually be required.

[1] National Defense Research Council, ''Physics of sound in the sea,'' Technical report, National Research Council, Peninsula Publishing, Los Altos, CA, 1946.

[2] R. J. Urick. *Principles of Underwater Sound* (McGraw-Hill, New York, 1983).

[3] D. R. Jackson, D. P. Winebrenner, and A. Ishimaru, ''Application of the composite roughness model to high-frequency bottom backscattering,'' J. Acoust. Soc. Am. **79**(5), 1410–1422 (1986).

[4] C. de Moustier and D. Alexandrou, ''Angular dependence of 12-kHz seafloor acoustic backscatter,'' J. Acoust. Soc. Am. **90**(1), 522–531 (1991).

[5] S. D. Morgera, ''Signal processing for precise ocean mapping,'' IEEE J. Ocean. Eng. **OE-1**(2), 49–57 (1976).

[6] S. D. Morgera and R. Sankar, ''Digital signal processing for precision wide-swath bathymetry,'' IEEE J. Ocean. Eng. **OE-9**(2), 73–84 (1984).

[7] M. V. Berry, ''On deducing the form of surfaces from their diffracted echoes,'' J. Phys. A **5**, 272–291 (1972).

[8] M. V. Berry, ''The statistical properties of echoes diffracted from rough surfaces,'' Philos. Trans. R. Soc. London, Ser. A **273**, 611–654 (1973).

[9] M. V. Berry and T. M. Blackwell, ''Diffractal echoes,'' J. Phys. A **14**, 3101–3110 (1981).

[10] N. F. Haines and D. B. Langston, ''The reflection of ultrasonic pulses from surfaces,'' J. Acoust. Soc. Am. **67**(5), 1443–1454 (1980).

[11] E. H. Nesbitt, ''Estimation of sea bottom parameters using acoustic backscattering at vertical incidence,'' Master's thesis, University of Washington, 1988.

[12] D. R. Jackson and E. Nesbitt, ''Bottom classification using backscattering at vertical incidence,'' J. Acoust. Soc. Am. Suppl. 1 **83**, S80 (1988).

[13] E. Pouliquen and X. Lurton, ''Identification de la nature du fond de la mer à l'aide de signaux d'écho-sondeurs. I. Modélisation d'échos réverbérés par le fond,'' Acta Acust. European Acoustics Assoc. **2**(2), 113–126 (1994).

[14] X. Lurton and E. Pouliquen, ''Identification de la nature du fond de la mer à l'aide de signaux d'écho-sondeurs. II. Méthode d'identification et résulatats experimentaux,'' Acta Acust. European Acoustics Assoc. **2**(3), 187–194 (1994).

[15] R. Chivers, N. Emerson, and D. R. Burns, ''New acoustic processing for underway surveying,'' Hydrographic J. **56**, 9–17 (1990).

Redistribution subject to ASA license or copyright; see http://acousticalsociety.org/content/terms. Download to IP: 132.177.229.80 On: Mon, 23 Nov 2015 20:45:01

[16] A. S. Tsehmahman, W. T. Collins, and B. T. Prager, ''Acoustic seabed classification and correlation analysis of sediment properties by QTC view,'' in Proceedings of IEEE OCEANS 97, pp. 921–926, 1997.
[17] E. L. Hamilton, ''Geoacoustic modeling of the sea floor,'' J. Acoust. Soc. Am. **68**(5), 1313–1340 (1980).
[18] E. L. Hamilton and R. T. Bachman, ''Sound velocity and related properties of marine sediments,'' J. Acoust. Soc. Am. **72**(6), 1891–1904 (1982).
[19] Applied Physics Laboratory. High-Frequency Ocean Environmental Acoustic Models Handbook. Technical report APL-UW TR9407 AEAS 9501, University of Washington, 1994.
[20] D. D. Sternlicht and C. P. de Moustier, ''Remote sensing of sediment characteristics by optimized echo envelope matching,'' J. Acoust. Soc. Am. **114**, 2727–2743 (2003).
[21] A. Ishimaru, *Wave Propogation and Scattering in Random Media* (Academic, New York, 1978), Vol. 2.
[22] T. H. Bell, Jr., ''Statistical features of sea-floor topography,'' Deep-Sea Res. Oceanogr. Abstr. **22**, 883–892 (1975).
[23] J. M. Berkson and E. Matthews, ''Statistical characterization of seafloor roughness,'' IEEE J. Ocean. Eng. **OE-9**(1), 48–51 (1984).
[24] C. G. Fox and C. E. Hayes, ''Quantitative methods for analyzing the roughness of the seafloor,'' Rev. Geophys. **23**(1), 1–48 (1985).
[25] D. R. Jackson, J. J. Crisp, and P. A. Thompson, ''High-frequency bottom backscatter measurements in shallow water,'' J. Acoust. Soc. Am. **80**(4), 1188–1199 (1986).
[26] K. B. Briggs, ''Microtopgraphical roughness of shallow-water continental shelves,'' IEEE J. Ocean. Eng. **14**(4), 360–367 (1989).
[27] D. R. Jackson and K. B. Briggs, ''High-frequency bottom backscattering: Roughness versus sediment volume scattering,'' J. Acoust. Soc. Am. **92**(2), 962–977 (1992).
[28] D. R. Jackson, K. B. Briggs, K. L. Williams, and M. D. Richardson, ''Test of models for high-frequency seafloor backscatter,'' IEEE J. Ocean. Eng. **21**(4), 458–470 (1996).
[29] E. L. Hamilton, ''Compressional wave attenuation in marine sediments,'' Geophysics **37**, 620–646 (1972).
[30] A. N. Ivakin and Y. P. Lysanov, ''Underwater sound scattering by volume inhomogeneities of a bottom medium bounded by a rough surface,'' Sov. Phys. Acoust. **27**(3), 212–215 (1981).
[31] J. H. Stockhausen, ''Scattering from the volume of an inhomogenous half-space,'' Technical Report 63/9, Naval Research Establishment, Dartmouth, N.S., Canada, August 1963.
[32] S. T. McDaniel and A. D. Gorman, ''An examination of the composite-roughness scattering model,'' J. Acoust. Soc. Am. **73**(5), 1476–1486 (1983).
[33] J. E. Moe and D. R. Jackson, ''Near-field scattering through and from a two-dimensional fluid–fluid rough interface,'' J. Acoust. Soc. Am. **103**(1), 275–287 (1998).
[34] P. Beckmann and A. Spizzichino, *The Scattering of Electromagnetic Waves from Rough Surfaces* (Macmillan, New York, 1963).
[35] L. M. Brekhovskikh and Y. P. Lysanov, *Fundamentals of Ocean Acoustics*, 2nd ed. (Springer, Berlin, 1991).
[36] L. A. Chernov, *Wave Propagation in a Random Medium, Part 2* (McGraw-Hill, New York, 1960).
[37] D. Tang, ''Small scale volumetric inhomogeneities of shallow water sediments: Measurements and discussion,'' in High Frequency Acoustics in Shallow Water, CP-45, pp. 539–546, Lerici, Italy, July 1997. NATO SACLANT Undersea Research Centre.
[38] J. A. Ogilvy, ''Computer simulation of acoustic wave scattering from rough surfaces,'' J. Phys. D **21**, 260–277 (1988).
[39] J. A. Ogilvy, *Theory of Wave Scattering from Random Rough Surfaces* (IOP, London, 1991).
[40] D. D. Sternlicht, ''High Frequency Acoustic Remote Sensing of Seafloor Characteristics,'' Ph.D. thesis, University of California, San Diego, 1999.
[41] S. Stanic, K. B. Briggs, P. Fleischer, W. B. Sawyer, and R. I. Ray, ''High-frequency acoustic backscattering,'' J. Acoust. Soc. Am. **85**(1), 125–136 (1989).
[42] S. Stanic, K. B. Briggs, P. Fleischer, R. I. Ray, and W. B. Sawyer, ''Shallow-water high-frequency bottom scattering off Panama City, Florida,'' J. Acoust. Soc. Am. **83**(6), 2134–2144 (1988).
[43] D. D. Sternlicht and C. P. de Moustier, ''Stacking and averaging techniques for bottom echo characterization,'' in Proceedings: 16th International Congress on Acoustics and 135th Meeting Acoustical Society of America, Vol. IV, pp. 3023–3024, Seattle, Washington, June 1998.

Redistribution subject to ASA license or copyright; see http://acousticalsociety.org/content/terms. Download to IP: 132.177.229.80 On: Mon, 23 Nov 2015 20:45:01